ACS APPLIED MATERIALS & INTERFACES

Research Article

www.acsami.org

Color-Switchable, Emission-Enhanced Fluorescence Realized by Engineering C-dot@C-dot Nanoparticles

Zhen Guo,*[,†] Zhiqiang Zhang,[†] Wei Zhang,[†] Lianqun Zhou,[†] Haiwen Li,[†] Hongmei Wang,[†] Caroline Andreazza-Vignolle,[‡] Pascal Andreazza,[‡] Dongxu Zhao,[§] Yihui Wu,[§] Quanlong Wang,[§] Tao Zhang,[†] and Keming Jiang[†]

[†]CAS Key Lab of Bio-Medical Diagnostics, Suzhou Institute of Biomedical Engineering and Technology, Chinese Academy of Sciences, No. 88, Keling Road, Suzhou New District 215163, People's Republic of China

[‡]Centre de Recherche sur la Matière Divisée, CRMD, UMR 6619 Université d' Orléans, CNRS, 1b rue de laférollerie, 45071 Orléans Cedex 2, France

[§]The State Key Laboratory of Luminescence and Applications, Changchun Institute of Optics, Fine Mechanics and Physics, Chinese Academy of Sciences, 3888 East Nan-Hu Road, Open Economic Zone, Changchun 130033, People's Republic of China

S *Supporting Information*

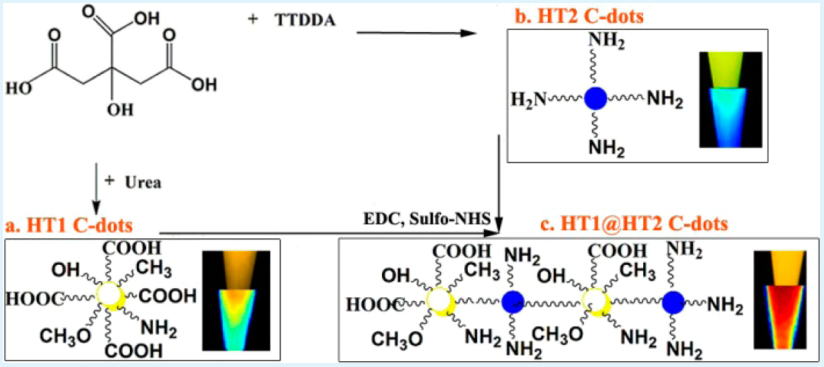

ABSTRACT: This paper reports the preparation and properties of color-switchable fluorescent carbon nanodots (C-dots). C-dots that emit dark turquoise and green−yellow fluorescence under 365 nm UV illumination were obtained from the hydrothermal decomposition of citric acid. Dark green fluorescent C-dots were obtained by conjugating prepared C-dots to form C-dot@C-dot nanoparticles. After successful conjugation of the C-dots, the fluorescence emission undergoes a blue-shift of nearly 20 nm (~0.15 eV) under UV excitation at 370 nm. The C-dots emit goldenrod, green−yellow, and gold light under excitation at 455 nm, which shows that the prepared C-dots are color-switchable. Furthermore, conjugation of the C-dots results in enhanced, red-shifted absorption of the $\pi-\pi^*$ transition of the aromatic sp^2 domains due to the conjugated π-electron system. N incorporation in the carbon structure leads to a degree of dipoles for all the aromatic sp^2 bonds. The enhanced absorption in a wide range from 226 to 601 nm indicates extended conjugation in the C-dot@C-dot structure. The time-resolved average lifetimes for the three different types of C-dots prepared in this study are 7.10, 7.65, and 4.07 ns. The radiative rate (reduced decay lifetime) increases when the C-dots are conjugated in the C-dot@C-dot nanoparticles, leading to the enhanced fluorescence emission. The fluorescence emission of the C-dot@C-dot nanoparticles can be used in applications such as flow cytometry and cell imaging.

KEYWORDS: *color switching, emission enhancement, fluorescent carbon nanodots, conjugating nanoparticles*

INTRODUCTION

Fluorescent C-dots are fascinating new materials with particle sizes on the order of several nanometers.[1−8] C-dot materials have attracted much attention because of their unique properties, such as water solubility, chemical inertness, low toxicity, easy fabrication, and low photobleaching. In addition to their use in multicolor photoluminescence (PL) bioimaging, C-dots can be used for glucose detection, nanocrystalline TiO_2 solar cells, label-free detection of Hg^{2+}, oxygen reduction, quantitative measurement of the intracellular pH of whole cells, hydrogen sulfide detection in aqueous media and inside live cells, and temperature probes, among other uses.[9−17] Excitation-, size-, and pH-dependent and excitation-independent fluorescent C-dots have been prepared.[18,19] However, the mechanisms related to the fluorescence emission properties of the C-dot nanomaterial still need further exploration; a few

Received: July 9, 2014
Accepted: November 19, 2014
Published: November 19, 2014

 © 2014 American Chemical Society

studies have reported the effects of different substances, such as silver and glass,[22] and of surface doping[23] on the fluorescence emission properties of C-dots. At present no study has investigated the effects of the interactions between C-dot nanoparticles on their fluorescence emission properties: wavelength and intensity modifications. The color-switching and emission properties of C-dots can be modified by engineering C-dot@C-dot nanoparticles. Until now C-dots can be synthesized by arc discharge,[1,24] laser ablation,[4,25] plasma treatment,[26] microwave methods,[9,27,28] and electrochemical synthesis.[29,30] Because thermal decomposition methods involve highly reactive species, easy solution control, low levels of air pollution, and low energy consumption, they can be used to prepare water-soluble C-dots without expensive experimental apparatus or complex, time-consuming isolation, purification, and functionalization procedures. This paper presents the preparation of dark turquoise and green−yellow luminescent C-dots (under 365 nm UV illumination) using a hydrothermal method and the tuning of the fluorescence emission properties by conjugating C-dots with a condensation reaction between carboxyl and amino groups on the different nanoparticle surfaces; the dark green fluorescent C-dots were obtained by conjugating C-dots to form C-dot@C-dot nanoparticles. The fluorescence spectra measurement demonstrates a blue-shift of nearly 20 nm under UV excitation at 370 nm for the conjugated C-dot nanoparticles, which shows that the prepared C-dots are color-switchable. Also, an increased radiative recombination rate was observed when the C-dots were conjugated in the C-dot@C-dot nanoparticles, which led to the enhanced fluorescence emission. Hence, they could be applied in flow cytometry and cell imaging. Further, the possible mechanisms related to the emission wavelength shift are discussed based on the conformational changes, the number of dangling bonds at the surface, and nanodot-confinement effects in the details. Taking account for the enhanced fluorescent emission of the C-dot@C-dot nanoparticles, factors such as interfacial interactions and the near-field enhancement were discussed as being responsible for the enhanced absorptions and emissions.

EXPERIMENTAL SECTION

Materials. Urea, citric acid monohydrate, and MES (2-(*N*-morpholino)ethanesulfonic acid monohydrate) were purchased from the Sinopharm Chemical Reagent Company, Shanghai. 4,7,10-Trioxa-1,13-tridecanediamine (TTDDA) was purchased from Sigma-Aldrich. NHS (*N*-hydroxysuccinimide) and EDC (1-ethyl-3-(3-(dimethylamino)propyl)carbodiimide) were purchased from Shanghai Medped Co., Ltd. Trypsin and Dulbecco's modified Eagle medium (DMEM) were purchased from Thermo Fisher Scientific Biochemical Product Co., Ltd. (Beijing). Fetal calf serum was purchased from Zhejiang Tianhang Biological Technology Co., Ltd. MCF-7 cells were purchased from Shanghai Life Science Cell Resource Center, Chinese Academy of Sciences. Polymer-coated super paramagnetic beads were purchased from Spherotech, Inc. All the chemical reagents were used without further purification.

Measurement Apparatus. Atomic force microscopy (AFM) measurements were performed using a Dimension Icon (Bruker AXS) instrument. X-ray diffraction (XRD) was performed using a Bruker Advance D8 X-ray diffractometer. Raman spectra were collected with a confocal Raman spectrometer (Labram HR 800) using a 532 nm laser as the excitation source. Transmission electron microscopy (TEM) measurements were performed with an FEI Tecnai G220 instrument. Fourier transform infrared (FTIR) spectra were recorded with a Nicolet 6700FTIR spectrometer. Fluorescent spectra were collected using a Hitachi F4600 spectrometer, and UV−vis absorption spectra were recorded on a PerkinElmer Lamda950 spectrophotometer. X-ray photoelectron spectroscopy (XPS) was performed using a Kratos Axis Ultra DLD multitechnique surface analyzer. Images of aqueous C-dots were captured using a CRI Maestro EXhigh-sensitivity optical imaging system for small animals. Fluorescence lifetimes were measured using a HORIBA Jobin Yvon FLtime-correlated single-photoncounting system. Optical images of magnetic beads coupled to the C-dots were obtained using a LeicaTCS SP5II laser confocal microscope with an argon laser light source (488 nm, 500 mW). An LSRFortessa flow cytometer (Becton Dickinson, BD) equipped with an argon laser (488 nm, 500 mW) was used to measure the fluorescence of the microbial cells. The parameters were acquired from pulse height signals of 5 000 events at a rate of ∼200 cells/s in the list mode. The samples were analyzed using a standard stream-in-air configuration. Magnetic beads labeled with C-dots were excited at 488 nm, and the emissions were measured at 515 nm.

Preparation of Fluorescent C-dot Particles. Citric acid and urea (mass ratio = 1:1) were dissolved in deionized water and magnetically stirred for 10 min to form a homogeneous solution. Then, 16 mL of the mixture was transferred to a 20 mL Teflon-lined stainless steel autoclave, which was heated at 180 °C for 1 h and then cooled to room temperature with running water. The resulting golden aqueous solution was labeled HT1 C-dots. Glycerin (15 mL) and 4,7,10-trioxa-1,13-tridecanediamine (TTDDA) were mixed to form a clear solution, which was heated to ∼180 °C under an argon atmosphere. Then, citric acid was quickly added to the hot solution, and the temperature was maintained at ∼180 °C for 1 h. After the mixture was cooled to room temperature, a dark brown solution was obtained and designated HT2 C-dots. The coupling reaction of an EDC, NHS, HT1, and HT2 C-dot mixture yielded the optimal conjugates. For the coupling reaction, aqueous HT1 and HT2 C-dots (volume ratio = 1:1, with the same concentration) were first transferred to an Eppendorf PCR (EP) tube. Then, NHS and EDC (volume ratio = 1:1, 10 mg/mL) were added, and the pH was adjusted to 5.5. The solution was mixed for 1 week, wrapped with black paper, and incubated at room temperature for 1 month. Under these reaction conditions, the HT1 C-dots attached to the HT2 C-dots, and the resulting sample was designated HT1@HT2 C-dots, as shown in Scheme 1. All obtained samples were subjected to dialysis for 2 days to remove smaller molecules and ions. To prepare magnetic beads labeled with fluorescent C-dots, C-dots and carboxyl-functionalized magnetic beads were reacted via the same overnight mixing procedure to yield the optimal conjugates.

Scheme 1. Preparation of HT1, HT2, and HT1@HT2 Fluorescent C-dots

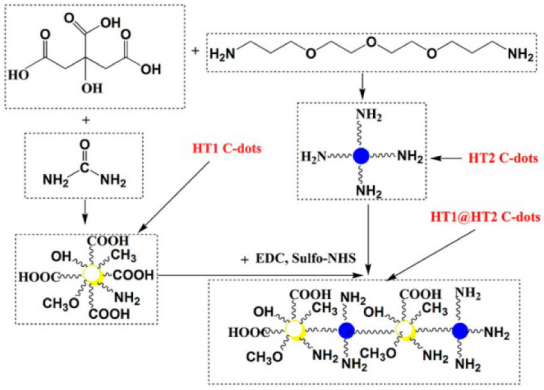

Preparation of Cells Labeled with C-dot Nanoparticles. For cell imaging, MCF-7 breast cancer cells were first placed in a multiwell plate and cultured for 2 days. Then, the cells were washed twice with phosphate-buffered saline (PBS) (pH = 7.4) following high-pressure disinfection. The MCF-7 cells were digested with 2.5% trypsin. Optical microscopy revealed that the cell morphology was round and the tentacles were retracted. When the trypsin finished performing the cell

dx.doi.org/10.1021/am5071078 | ACS Appl. Mater. Interfaces 2014, 6, 20700−20708

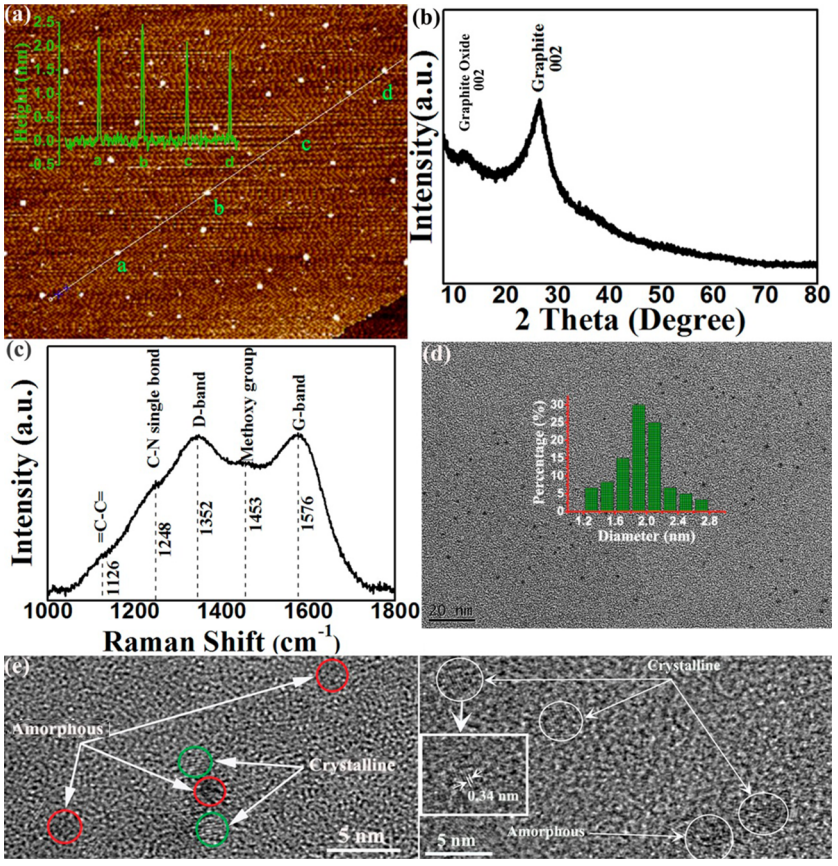

Figure 1. (a) AFM image of the C-dots; the superimposed image is the height profile of the C-dots dispersed on fresh mica substrate along the line marked in the AFM image. (b, c) 2Theta XRD pattern and Raman spectrum of the C-dots. (d) TEM image of the C-dots; insert: statistical distribution of the C-dots in the TEM image. (e) HRTEM image of the crystalline and amorphous C-dots; the inset in a square frame shows the enlarged HRTEM image of the C-dot nanoparticle with *d* spacing value of 0.34 nm.

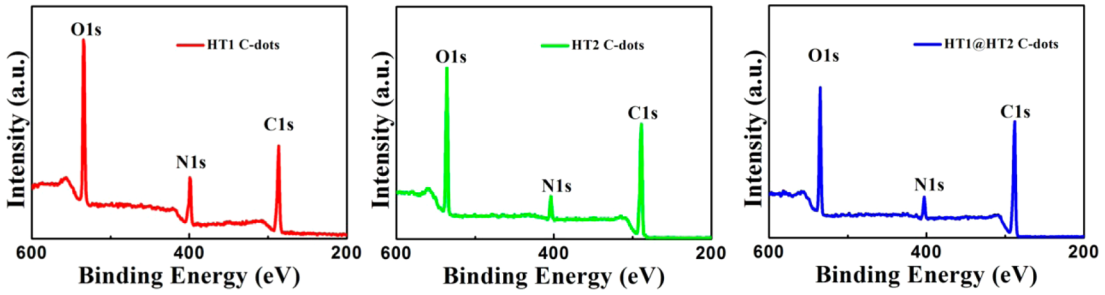

Figure 2. XPS spectra of the HT1, HT2, and HT1@HT2 C-dots, respectively.

digestion, the digestion was terminated using media (Dulbecco's modified Eagle medium (DMEM) + 10% fetal calf serum), and the cell concentration was ~$5 \times 10^3/\mu$L. Then the cells were cultured with the C-dot@C-dot nanoparticles (37 °C, 8 h) for the fluorescent imaging.

RESULTS AND DISCUSSION

The AFM image and corresponding height analysis shown in Figure 1a show that the hydrothermally synthesized C-dots are well-dispersed on the freshly cleaved mica substrate. The height profile along a given line reveals that the C-dot diameter ranges from 1.25 to 2.75 nm with a mean size of 1.879 nm (Figures S1 and S2, Supporting Information). The XRD patterns of the dry C-dots are presented in Figure 1b and have two peaks at 11.7° and 26.5° that correspond to *d* spacings of 7.2 and 3.4 Å, respectively. The weak-intensity reflection at 2θ = 11.7° is attributed to the (002) lattice spacing (7.2 Å) of graphite oxide,[31−33] indicating that the C-dots are partially oxidized. The sharp, high-intensity reflection at d_{002} = 3.4 Å, which is very close to the graphite (002) lattice spacing,[7,34−36] indicates the formation of C-dots. The Raman spectra (λ_{ex} = 532 nm) of the prepared C-dots (Figure 1c) exhibit two broad peaks at approximately 1346 and 1576 cm^{-1}, which are attributed to the D (sp^3-hybridized) and G (sp^2-hybridized) bands, respectively. The D band is associated with the vibrations of carbon atoms with dangling bonds in the termination plane of disordered graphite or glassy carbon. The G band corresponds to the E_{2g} mode of graphite and is related to the vibration of sp^2-hybridized carbon atoms in a two-dimensional hexagonal lattice.[37] The intensity ratio of the disordered D band to the crystalline G band (I_D/I_G) is ~0.9958 for the C-dots, indicating that they have a structure similar to graphite. The C-dots are partially oxidized, which initially results in structural defects,

dx.doi.org/10.1021/am5071078 | ACS Appl. Mater. Interfaces 2014, 6, 20700−20708

such as oxygenated groups (C−O, C═O, O−C═O) in the sp^2 carbon site, and then leads to vacant lattice sites and sp^3 carbon.[3] The weak peak between the D and G bands at 1453 cm^{-1} is attributed to the asymmetric bending of the methyl group.[38,39] The characteristic peak of covalent C−N single bonds at 1248 cm^{-1} is also observed in the Raman spectrum.[40] The shoulder peak at 1126 cm^{-1} is attributed to the presence of ═C—C═ bonds.[41] As shown in Figures 1d and S3 (in the Supporting Information), the mean size of the C-dots is 1.941 nm with size distribution ranging from 1.28 to 2.78 nm, which illustrates good accordance with the statistical distribution of the AFM results. The high-resolution TEM (HRTEM) image shown in Figure 1e reveals the presence of both amorphous and graphite phases. Well-resolved lattice fringes are observed in the HRTEM image shown in Figure 1e; these fringes correspond to a *d* spacing of 0.34 nm, which is close to the value for the (002) plane of graphitic carbon,[24] indicating that the C-dots have a partially graphitic structure.

The elemental composition and type of chemical bonds in the HT1, HT2, and HT1@HT2 C-dots were analyzed with XPS as shown in Figure 2. The peaks at 284.7, 399.0, and 530.6 eV are attributed to the C 1s, N 1s, and O 1s emissions, respectively. The N/O ratios are 0.33, 0.25, and 0.28 for the HT1, HT2, and HT1@HT2 C-dots, respectively, indicating that more N atoms are substitutionally doped into the HT1 C-dots than into the HT2 and HT1@HT2 C-dots. The C/O ratios are 0.67, 0.49, and 0.77 for the HT1, HT2, and HT1@HT2 C-dots, respectively, demonstrating that other atoms might replace a fraction of the O atoms when the HT1 and HT2 C-dots are coupled in the HT1@HT2 C-dots. As shown in Figures S4, Supporting Information, the main peak in the high-resolution C 1s XPS spectra of the HT1, HT2, and HT1@HT2 C-dots is observed at 284.7 eV and corresponds to the sp^2/sp^3 C═C/C−C atoms. The sp^3 C−N/C−O peak is observed at ∼286 eV, and the relative intensity ratios of the main peak to the sp^3 peak are 2.02, 1.16, and 1.47 for the HT1, HT2, and HT1@HT2 C-dots, respectively, with the ratio for the conjugated HT1@HT2 C-dots nanoparticles falling between those for the HT1 and HT2 C-dots. The sp^2 C═O peak at ∼288 eV further demonstrates that different structural bonds, namely, C—C/C═C, C—N, C—O, and C═O bonds, exist in the C-dots.[42] The N 1s spectra of the N-doped samples were fine-scanned and deconvoluted into three bands at ∼399.0, ∼400.0, and ∼401−403 eV (Figure S4, Supporting Information), which correspond to pyridinic N (N bonded to two C nearest neighbors), pyrrolic N (N part of a pentagon ring connected to two C), and graphitic N (N bonded to three C nearest neighbors), respectively. These bands are due to N atoms in a π-conjugated system that contribute one or two π electrons to it.[43−45] The variation in the localized π electronic states near the Fermi level at the carbon atoms might result in a shift in the binding energy from 402.1 to 401.5 eV for the graphitic N species in the HT1@HT2 C-dot nanoparticles. The shift in the N 1s binding energy of the graphitic N to a lower energy is consistent with the presence of a negatively charged N (a shift in the N 1s binding energy of the graphitic N to a higher energy is expected for a positively charged N). If N is negatively charged, the surrounding carbon atoms are positively charged because of the screening effect. The positive charge on the carbon, which is due to the electron transfer from the N atom to the π conjugated state, can explain the shift in the carbon localized π state from the Fermi level to a lower energy level.[46]

The C-dot surface functional groups were determined by analyzing the HT1, HT2, and HT1@HT2 C-dot FTIR spectra (Figure 3).The broad absorption bands between 3000 and 3500

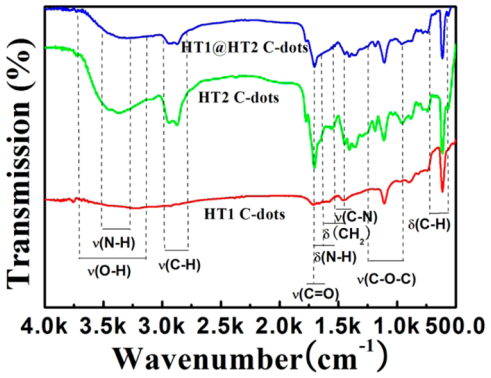

Figure 3. FTIR spectra of the HT1, HT2, and HT1@HT2 C-dots.

cm^{-1} are assigned to ν(O−H) and ν(N−H). These functional groups improve the hydrophilicity and stability of the C-dots in aqueous systems.[7] Asymmetric and symmetric C—O—C stretching vibrations (approximately 1292 and 1193 cm^{-1}, respectively) and ν(C═O) stretching vibrations (1650 cm^{-1}) are detected.[4] The peaks at 1530 and 1660 cm^{-1} are assigned to amide stretching vibrations, and the peak at 1455 cm^{-1} is attributed to the amide C—N stretch. For the HT2 C-dots with TTDDA molecules, the carbonyl moieties react with the TTDDA amine head groups to form amides on the C-dots.[14,47] For the HT1 C-dots, the carboxyl and amide groups on the C-dot surface can be functionalized with urea molecules.[7] The N—H, O—H, and C═O absorption peak intensities of the HT1@HT2 C-dots are weaker than those of the HT2 C-dots (but stronger than those of the HT1 C-dots), which provides further evidence of the conjugation of the HT1 and HT2 C-dot nanoparticles.

The UV−vis absorption and fluorescence spectra of the dilute HT1, HT2, and HT1@HT2 C-dot aqueous solutions are shown in Figure 4a−c. The two HT1 C-dot absorption peaks at ∼335 nm (3.69 eV) and ∼235 nm (5.27 eV) are attributed to photoabsorption from the lowest molecular orbital to the σ and π orbitals (highest molecular orbitals). The typical absorption band at 235 nm is assigned as the $\pi-\pi^*$ transition of the aromatic sp^2 domains.[19,48] The HT2 C-dot $\pi-\pi^*$ peak is small, indicating that this transition is weak. For the HT1@HT2 C-dots, the $\pi-\pi^*$ absorption peak is red-shifted to 250 nm and increases in intensity due to the conjugated π-electron system.[49] The N incorporated into the carbon structures leads to a degree of dipoles for all the aromatic sp^2 bonds, and a permanent dipole effect could lead to the increase in the $\pi-\pi^*$ absorption. In addition, the absorption band at ∼335 nm could be due to the surface carboxyl, amino, and other groups that passivate the surface traps.[19−21,48] The surface traps are at different energy levels below the highest occupied molecular orbital (HOMO), resulting in various transition modes as shown by the excitation-dependent fluorescence emission spectra. Furthermore, n-π^* transitions are observed for the HT1, HT2, and HT1@HT2 C-dots.[42] Notably, the n-π^* transition mode of the HT1@HT2 C-dots exhibits an asymmetric absorption peak as shown in Figure 4c. In addition to the absorption peak at 336 nm, another shoulder peak is observed at ∼366 nm. These absorptions are typical for aromatic π systems with extended

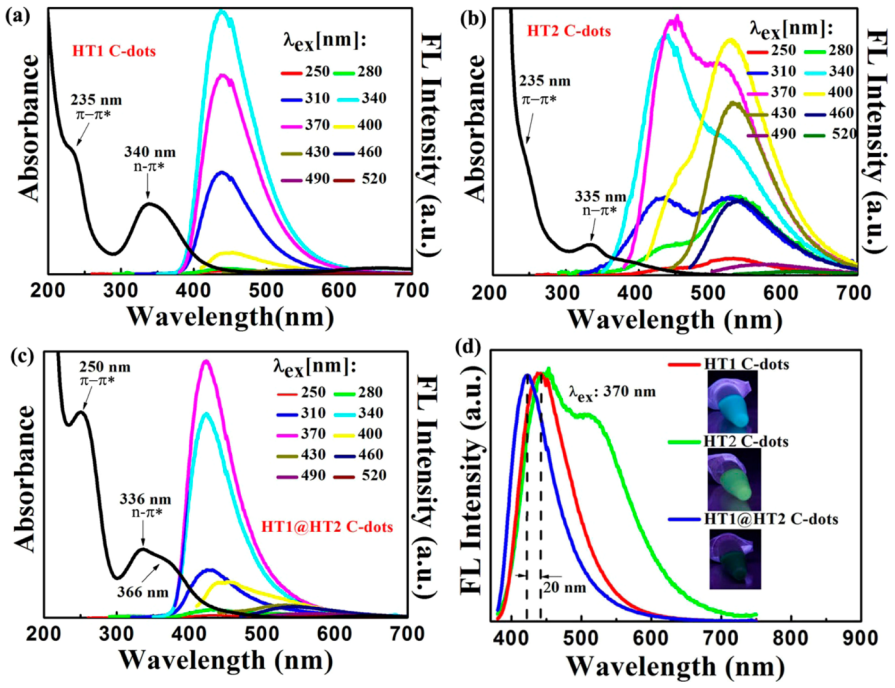

Figure 4. (a−c) UV−vis absorption (black solid lines) and photoluminescence spectra of HT1, HT2, and HT1@HT2 C-dots under different excitation wavelengths; the insets show the corresponding normalized photoluminescence spectra. (d) Photoluminescence spectra of HT1, HT2, and HT1@HT2 C-dots under UV excitation of 370 nm; the insets show the photoimages under UV lamp of 365 nm.

conjugation as in the C-dot structure. The dominant fluorescence emission peak of the HT1 C-dots at 440 nm (~2.82 eV) does not shift as the excitation wavelength is increased from 250 to 370 nm, which indicates that the C-dot surfaces are relatively uniform and well-passivated in a certain degree.[50] A red-shift from 440 to 619 nm (~2.00 eV) is observed as the excitation wavelength is increased from 400 to 520 nm, which can be explained by multiple transition modes. For the HT2 C-dots, two emission peaks are observed as the excitation wavelength is increased from 250 to 400 nm. The dominant emission peak at 530 nm (~2.34 eV) and shoulder peak at ~440 nm are observed under excitation at 250 and 280 nm. A peak with almost the same intensity as the 530 nm peak is observed at 440 nm under excitation at 310 nm. Increasing the excitation wavelength from 340 to 400 nm results in a blue-shift of the emission peak from 440 to 460 nm (~2.69 eV). A red-shift from 530 to 619 nm (~2.00 eV) is observed as the excitation wavelength is increased from 400 to 520 nm. The HT1@HT2 C-dot emission spectra differ from the HT1 and HT2 C-dot emission spectra in that the dominant emission peak is blue-shifted by ~20 nm (0.15 eV) under excitation at 370 nm (Figure 4d). The blue-shift is mainly due to the following factors: (1) Conformational changes can blue-shift the fluorescence emission to a higher energy and lead to a narrower emission bandwidth (the full width at half maximum (fwhm) values of the fluorescence spectra excited under 370 nm radiation were 83.52, 156.01, and 69.86 nm for the HT1, HT2, and HT1@HT2 C-dot samples, respectively). The blue-shifted spectra are indicative of a significant amount of disorder or strain that would cause some nonplanarity in the conjugated system. Thus, the emission is blue-shifted due to a lack of strong cofacial $\pi-\pi$ alignment and the existence of strong C-dot@C-dot interactions through the conjugation bonds. The close packing of the two fluorescent units probably enhances the electronic interactions between stacked π electrons. The conformational twisting of the conjugated C-dot@C-dot nanoparticles in the aggregate state might therefore be responsible for the enhanced, blue-shifted fluorescence emission that is observed for the π conjugated C-dot nanoparticles.[51,52] (2) The blue-shift is also due to the decrease in the number of dangling bonds at the surface that results from conjugating the C-dots (Figure S5, Supporting Information). The band structure of nanostructured C-dot materials is sensitive to the type of surface passivation, and the effective bandgap can be reduced by the presence of dangling bonds at the surface that result from incomplete passivation.[53,54] (3) Due to nanodot-confinement effects, the emission color can be modified by the interface states. By coupling nonradiative modes to radiation and modifying the boundary conditions of the electromagnetic field, conjugated interfaces might alter both the radiative decay rate and the spatial distribution of the emitted radiation, and the excited molecule could transfer energy to the interface radiatively.[55−57] The inserted images in Figure 4d show that, under UV irradiation at 365 nm, the HT1, HT2, and HT1@HT2 C-dots are dark turquoise, green−yellow, and dark green, respectively. When the aqueous C-dots solution was used as fluorescent ink written on the filter paper under UV irradiation at 254 nm, sky blue, pale green, and dark slate gray emission colors could be observed (Figures S6, Supporting Information). These results indicate that the emission colors can be tuned by engineering the C-dot@C-dot nanoparticles. As shown in Figure S7, Supporting Information, the shoulder emission peak intensities of the HT1@HT2 C-dots are different from those of the HT1 and HT2 C-dots, but the HT1@HT2 C-dots exhibit some of the fluorescence emission characteristics of the HT1 and HT2 C-dots under excitation at 400 and 430 nm. However, because the emission energy levels under excitation at >460 nm are similar, the HT1@HT2 C-dots exhibit nearly the same fluorescence emission spectra as the other samples. Notably, given the large

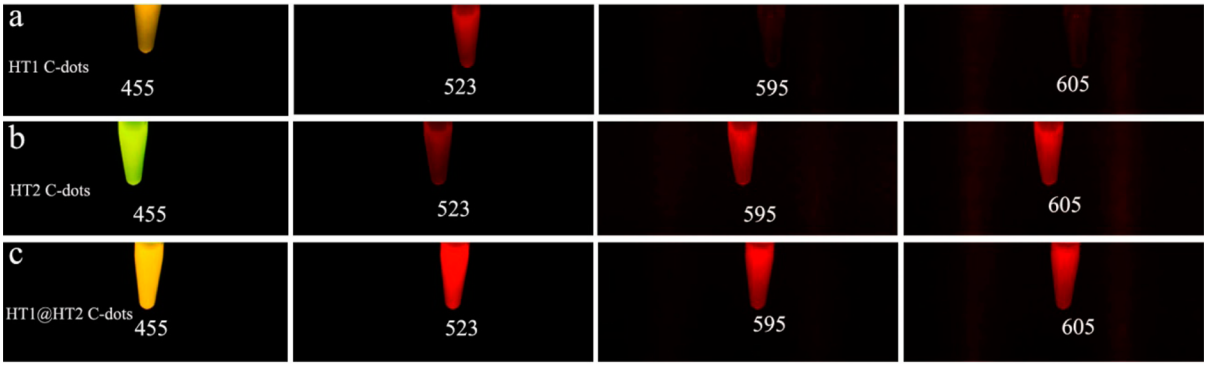

Figure 5. (a–c) Photoimages of aqueous solution of the HT1, HT2, and HT1@HT2 C-dots samples captured under different wavelengths through corresponding long-pass filters, respectively.

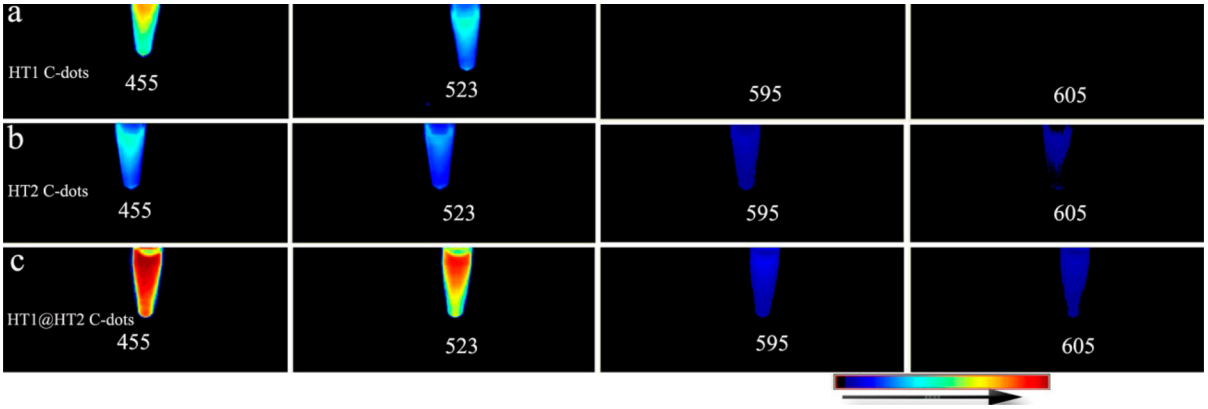

Figure 6. (a–c) Fluorescent intensity measurement of aqueous solution of the HT1, HT2, and HT1@HT2 C-dots samples, respectively, captured under different wavelengths through corresponding long-pass filters with the same exposure time of 500 ms.

number of surface and interface energy traps, the fluorescence emission spectra depend on the excitation wavelength. Under excitation at 455 nm, golden rod, green–yellow, and gold emissions are observed for the HT1, HT2, and HT1@HT2 C-dots, respectively (Figure 5a–c). When the three samples are excited at wavelengths > 523 nm, only red emissions are observed, which is consistent with the fluorescence measurements.

In addition to emission color tuning by conjugating C-dot nanoparticles, the fluorescence emissions were enhanced by increasing the excitation wavelength from 455 to 605 nm (Figure 6a–c).The enhanced fluorescence emission of the HT1@HT2 C-dots is clearly captured by a charge-coupled device (CCD) camera, further demonstrating the conjugation of these nanoparticles, which results in stronger recombination for photon emission. Because certain HT1 and HT2 C-dot energy levels benefit from radiation recombination during conjugation and therefore introduce new transition modes, the observed absorption spectrum of the HT1@HT2 C-dots differs from those of the HT1 and HT2 C-dots. The new conjugation structure improves the electron mobility of the photoexcited charge carriers. Consequently, the probability of an electron transition from the ground state to the lowest excited singlet state should be higher.[58]

The absorption intensity of the n-π^* transition is enhanced for the HT1@HT2 C-dots (Figure S5, Supporting Information). Additionally, the enhancement of the electron cloud activity results in a narrower energy gap, which probably contributes to the red-shift of the π–π^* absorption peak of the HT1@HT2 C-dots. These absorption peaks indicate extended conjugation in the C-dot@C-dot structure. The high-energy tail in the visible region of the C-dot absorption spectrum is attributed to Mie scattering caused by the particles.[59,60] Therefore, the absorption is stronger for the HT1@HT2 C-dots. The time-resolved average lifetimes of the HT1, HT2, and HT1@HT2 C-dots are 7.10, 7.65, and 4.07 ns, respectively (Figure 7). The shorter fluorescence decay lifetime of the HT1@HT2 C-dots illustrates the good conjugation between the HT1 and HT2 C-dots. Electron-donating groups on the C-dots can enhance the degree of conjugation and are expected to increase the transition probability from the excited states to the ground state, resulting in strong recombination for photon emissions.[19] Both C-dots and quantum dots, for which radiative

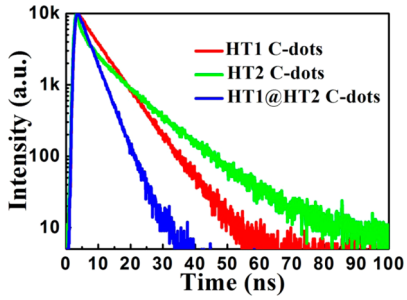

Figure 7. Fluorescence lifetime decay profiles of HT1, HT2, and HT1@HT2 C-dots with excitations at 370 nm; emission monitored at 440 nm.

recombination of excitons is the widely accepted luminescence mechanism, require surface passivation for fluorescence.[37] The enhanced fluorescence emission of conjugated C-dots shows that aqueous nanoparticles undergo very strong electronic transitions.[2] No classical bandgap absorptions are observed for C-dots. Therefore, the surface or newly built interface states should be accessed directly from the ground state, and the interfacial interactions responsible for the enhanced absorptions and emissions probably trap an increasing amount of excited-state energy. The nonradiative decay is slowed by the formation of C-dot@C-dot nanoparticle clusters or aggregates (Figure S8, Supporting Information), leading to enhanced luminescence.[56,57] The fluorescence resonance energy transfer (FRET) between the C-dot@C-dot nanoparticles was investigated to determine their relative proximity. The absorption spectra of the HT1, HT2, and HT1@HT2 C-dot samples are presented in Figure S9, Supporting Information; the spectral overlap meets the FRET requirements, which should allow for efficient enhancement of the fluorescence.[61−65] In addition, the near-field enhancement (NFE) synergistically improves the emission intensity of the C-dot@C-dot nanoparticles when the two luminescent nanoparticles are located at an optimum distance from each other.[66] These enhanced fluorescence properties make the C-dot nanoparticles particularly valuable for optical bioimaging in vitro and in vivo, especially considering the emerging need for molecular probes in high-resolution cellular imaging.[67,68]

To explore the fluorescent properties of the as-prepared C-dots for potential applications in flow cytometry, the HT2 C-dots were conjugated to magnetic beads functionalized with carboxyl groups, and then the HT1 C-dots were attached to the HT2 C-dots to improve the fluorescence emission. The flow cytometry results are consistent with the previous observations. The fluorescence emission of the HT2 C-dots conjugated to magnetic beads (sample C) was detected by the detector (Figure S10, Supporting Information). Combining the HT1 C-dots with the magnetic bead-HT2 C-dot conjugates (sample D) results in an enhanced fluorescence intensity. The laser confocal fluorescence microscopy images show that the conjugation of the magnetic beads with the fluorescent HT1 and HT2 C-dots is successful (Figure S11, Supporting Information). The fluorescence microscopy image shown in Figure S10a, Supporting Information, demonstrates that magnetic beads can be successfully conjugated to C-dots. The conjugation enables the C-dots to covalently attach to the magnetic beads to form fluorescent labels. The HT1 C-dots conjugated with magnetic beads exhibit a slightly enhanced fluorescence intensity compared to the background. Therefore, the prepared HT1 C-dots might have fewer amino groups on the surface than the HT2 C-dots, as strongly indicated by the weak amide FTIR absorption band for the HT1 C-dots compared to the strong band observed for the HT2 C-dots. These results indicate that the carboxyl group-modified HT1 C-dots can be strongly coupled to the amide group-modified HT2 C-dots, which suggests that the fundamental unit formed via conjugation is magnetic bead−HT2 C-dot−HT1 C-dot. The presence of these functional groups makes the C-dots water-soluble, which is essential for biological work. These groups also provide a convenient way to functionalize the surface, which can be easily accomplished using well-established conjugation protocols. To assess the potential of the C-dot@C-dot nanoparticles for bioimaging applications, the prepared HT1@HT2 C-dots were introduced into MCF-7 breast cancer cells to examine their imaging capabilities using an in vitro biomicroscopy test. The fluorescence emission is observed in the cell membrane and cell cytoplasm and is slightly weaker in the center, indicating that the C-dot@C-dot nanoparticles easily penetrate into the cell (Figure S12, Supporting Information). Sedimentation, endocytosis, and the diffusion mechanisms by which the cells uptake the C-dots might play an important role,[69,70] but further investigations are needed to understand the endocytosis mechanism. The C-dots might successfully accumulate in the cell and its nucleus by binding to facilitator proteins or peptides that cross cell membrane barriers more readily for a longer time. Because specific interactions with different species, hindrance by mobile and immobile obstacles, and collisions with other proteins and barriers such as cytoskeletal filaments affect the C-dot mobility, most of the C-dots diffuse in the cells more slowly than expected for random Brownian motion.

CONCLUSIONS

In summary, dark turquoise and green−yellow fluorescent C-dots were prepared by hydrothermal decomposition, and engineering C-dot@C-dot nanoparticles resulted in color-switchable C-dots. The new transition modes of the conjugated C-dot@C-dot nanoparticles lead to a blue-shift of nearly 20 nm (~0.15 eV) under UV excitation at 370 nm. Conjugation of the C-dot@C-dot nanoparticles results in enhanced absorption by of the aromatic sp^2 domain transition, and the absorption peaks indicate extended conjugation in the C-dot@C-dot structure. The C-dot@C-dot nanoparticles exhibit enhanced fluorescence emission because of an increase in the absorption with a broad range and a decrease in the decay lifetime. The fluorescent C-dots conjugated to magnetic beads have potential for use in flow cytometry. These magnetic beads might also be employed in cell separation, quantitative measurement of the intracellular pH of whole cells, etc. The color-switchable, emission-enhanced fluorescent C-dot@C-dot nanoparticles could be successfully applied for bioimaging applications; however, further experiments should be carried out to explore the endocytosis and the diffusion mechanisms of the nanoparticles uptake by the cells.

ASSOCIATED CONTENT

Supporting Information

Supporting AFM, TEM, and XPS, and fluorescence spectra. This material is available free of charge via the Internet at http://pubs.acs.org.

AUTHOR INFORMATION

Corresponding Author

*Tel.: 86-512-69588058. Fax: 86-512-69588058. E-mail: guozhen@sibet.ac.cn or happygzh2000@163.com.

Notes

The authors declare no competing financial interest.

ACKNOWLEDGMENTS

This work is supported by the National Natural Science Foundation of China under Grant Nos. 51202154, 51405483, and 51205268; the Natural Science Foundation of Jiangsu Province under Grant Nos. BK20131169, BK20140377, and BK2012190; National 863 Key Project under Grant No. 2012AA040503; the Science Technology development program of Suzhou City under Grant No. ZXY2012011; the Nano-

technology for special project of Suzhou City under Grant No. ZXG2013038; and the SRF for ROCS, SEM.

REFERENCES

(1) Xu, X. Y.; Ray, R.; Gu, Y. L.; Ploehn, H. J.; Gearheart, L.; Raker, K.; Scrivens, W. A. Electrophoretic Analysis and Purification of Fluorescent Single-Walled Carbon Nanotube Fragments. *J. Am. Chem. Soc.* **2004**, *126*, 12736−12737.

(2) Wang, X.; Cao, L.; Yang, S. T.; Lu, F. S.; Meziani, M. J.; Tian, L. L.; Sun, K. W.; Bloodgood, M. A.; Sun, Y. P. Bandgap-Like Strong Fluorescence in Functionalized Carbon Nanoparticles. *Angew. Chem., Int. Ed.* **2010**, *49*, 5310−5314.

(3) Zhao, Q. L.; Zhang, Z. L.; Huang, B. H.; Peng, J.; Zhang, M.; Pang, D. W. Facile Preparation of Low Cytotoxicity Fluorescent Carbon Nanocrystals by Electrooxidation of Graphite. *Chem. Commun.* **2008**, 5116−5118.

(4) Hu, S. L.; Niu, K. Y.; Sun, J.; Yang, J.; Zhao, N. Q.; Du, X. W. One-Step Synthesis of Fluorescent Carbon Nanoparticles by Laser Irradiation. *J. Mater. Chem.* **2009**, *19*, 484−488.

(5) Peng, H.; Travas-Sejdic, J. Simple Aqueous Solution Route to Luminescent Carbogenic Dots from Carbohydrates. *Chem. Mater.* **2009**, *21*, 5563−5565.

(6) Baker, S. N.; Baker, G. A. Luminescent Carbon Nanodots: Emergent Nanolights. *Angew. Chem., Int. Ed.* **2010**, *49*, 6726−6744.

(7) Qu, S. N.; Wang, X. Y.; Lu, Q. P.; Liu, X. Y.; Wang, L. J. A Biocompatible Fluorescent Ink Based on Water-Soluble Luminescent Carbon Nanodots. *Angew. Chem., Int. Ed.* **2012**, *51*, 12215−12218.

(8) Park, S. Y.; Lee, H. U.; Park, E. S.; Lee, S. C.; Lee, J.-W.; Jeong, S. W.; Kim, C. H.; Lee, Y.-C.; Huh, Y. S.; Lee, J. Photoluminescent Green Carbon Nanodots from Food-Waste-Derived Sources: Large-Scale Synthesis, Properties, and Biomedical Applications. *ACS Appl. Mater. Interfaces* **2014**, *6*, 3365−3370.

(9) Liu, C. J.; Zhang, P.; Tian, F.; Li, W. C.; Li, F.; Liu, W. G. One-Step Synthesis of Surface Passivated Carbon Nanodots by Microwave Assisted Pyrolysis for Enhanced Multicolor Photoluminescence and Bioimaging. *J. Mater. Chem.* **2011**, *21*, 13163−13167.

(10) Shi, W. B.; Wang, Q. L.; Long, Y. J.; Cheng, Z. L.; Chen, S. H.; Zheng, H. Z.; Huang, Y. M. Carbon Nanodots as Peroxidase Mimetics and Their Applications to Glucose Detection. *Chem. Commun.* **2011**, *47*, 6695−6697.

(11) Mirtchev, P.; Henderson, E. J.; Soheilnia, N.; Yip, C. M.; Ozin, G. A. Solution Phase Synthesis of Carbon Quantum Dots as Sensitizers for Nanocrystalline TiO2 Solar Cells. *J. Mater. Chem.* **2012**, *22*, 1265−1269.

(12) Zhou, L.; Lin, Y. H.; Huang, Z. Z.; Ren, J. S.; Qu, X. G. Carbon Nanodots as Fluorescence Probes for Rapid, Sensitive, and Label-Free Detection of Hg2+ and Biothiols in Complex Matrices. *Chem. Commun.* **2012**, *48*, 1147−1149.

(13) Zhu, C. Z.; Zhai, J. F.; Dong, S. J. Bifunctional Fluorescent Carbon Nanodots: Green Synthesis Via Soy Milk and Application as Metal-Free Electrocatalysts for Oxygen Reduction. *Chem. Commun.* **2012**, *48*, 9367−9369.

(14) Shi, W.; Li, X. H.; Ma, H. M. A Tunable Ratiometric Ph Sensor Based on Carbon Nanodots for the Quantitative Measurement of the Intracellular Ph of Whole Cells. *Angew. Chem., Int. Ed.* **2012**, *51*, 6432−6435.

(15) Yu, C. M.; Li, X. Z.; Zeng, F.; Zheng, F. Y.; Wu, S. Z. Carbon-Dot-Based Ratiometric Fluorescent Sensor for Detecting Hydrogen Sulfide in Aqueous Media and inside Live Cells. *Chem. Commun.* **2013**, *49*, 403−405.

(16) Chen, P. C.; Chen, Y. N.; Hsu, P. C.; Shih, C. C.; Chang, H. T. Photoluminescent Organosilane-Functionalized Carbon Dots as Temperature Probes. *Chem. Commun.* **2013**, *49*, 1639−1641.

(17) Qian, Z.; Shan, X.; Chai, L.; Ma, J.; Chen, J.; Feng, H. Si-Doped Carbon Quantum Dots: A Facile and General Preparation Strategy, Bioimaging Application, and Multifunctional Sensor. *ACS Appl. Mater. Interfaces* **2014**, *6*, 6797−6805.

(18) Li, H. T.; He, X. D.; Kang, Z. H.; Huang, H.; Liu, Y.; Liu, J. L.; Lian, S. Y.; Tsang, C. H. A.; Yang, X. B.; Lee, S. T. Water-Soluble Fluorescent Carbon Quantum Dots and Photocatalyst Design. *Angew. Chem., Int. Ed.* **2010**, *49*, 4430−4434.

(19) Li, X. M.; Zhang, S. L.; Kulinich, S. A.; Liu, Y. L.; Zeng, H. B. Engineering Surface States of Carbon Dots to Achieve Controllable Luminescence for Solid-Luminescent Composites and Sensitive Be2+ Detection. *Sci. Rep.* **2014**, *4*, 4976.

(20) Shi, Q. Q.; Li, Y. H.; Xu, Y.; Wang, Y.; Yin, X. B.; He, X. W.; Zhang, Y. K. High-Yield and High-Solubility Nitrogen-Doped Carbon Dots: Formation, Fluorescence Mechanism and Imaging Application. *RSC Adv.* **2014**, *4*, 1563−1566.

(21) Qu, D.; Zheng, M.; Du, P.; Zhou, Y.; Zhang, L. G.; Li, D.; Tan, H. Q.; Zhao, Z.; Xie, Z. G.; Sun, Z. C. Highly Luminescent S, N Co-doped Graphene Quantum Dots with Broad Visible Absorption Bands for Visible Light Photocatalysts. *Nanoscale* **2013**, *5*, 12272−12277.

(22) Zhang, Y. X.; Goncalves, H.; da Silva, J. C. G. E.; Geddes, C. D. Metal-Enhanced Photoluminescence from Carbon Nanodots. *Chem. Commun.* **2011**, *47*, 5313−5315.

(23) Xu, J.; Sahu, S.; Cao, L.; Bunker, C. E.; Peng, G.; Liu, Y. M.; Fernando, K. A. S.; Wang, P.; Guliants, E. A.; Meziani, M. J.; Qian, H. J.; Sun, Y. P. Efficient Fluorescence Quenching in Carbon Dots by Surface-Doped Metals—Disruption of Excited State Redox Processes and Mechanistic Implications. *Langmuir* **2012**, *28*, 16141−16147.

(24) Shen, J. H.; Zhu, Y. H.; Yang, X. L.; Li, C. Z. Graphene Quantum Dots: Emergent Nanolights for Bioimaging, Sensors, Catalysis and Photovoltaic Devices. *Chem. Commun.* **2012**, *48*, 3686−3699.

(25) Sun, Y. P.; Zhou, B.; Lin, Y.; Wang, W.; Fernando, K. A. S.; Pathak, P.; Meziani, M. J.; Harruff, B. A.; Wang, X.; Wang, H. F.; Luo, P. J. G.; Yang, H.; Kose, M. E.; Chen, B. L.; Veca, L. M.; Xie, S. Y. Quantum-Sized Carbon Dots for Bright and Colorful Photoluminescence. *J. Am. Chem. Soc.* **2006**, *128*, 7756−7757.

(26) Gokus, T.; Nair, R. R.; Bonetti, A.; Bohmler, M.; Lombardo, A.; Novoselov, K. S.; Geim, A. K.; Ferrari, A. C.; Hartschuh, A. Making Graphene Luminescent by Oxygen Plasma Treatment. *ACS Nano* **2009**, *3*, 3963−3968.

(27) Zhai, X. Y.; Zhang, P.; Liu, C. J.; Bai, T.; Li, W. C.; Dai, L. M.; Liu, W. G. Highly Luminescent Carbon Nanodots by Microwave-Assisted Pyrolysis. *Chem. Commun.* **2012**, *48*, 7955−7957.

(28) Jiang, J.; He, Y.; Li, S. Y.; Cui, H. Amino Acids as the Source for Producing Carbon Nanodots: Microwave Assisted One-Step Synthesis, Intrinsic Photoluminescence Property and Intense Chemiluminescence Enhancement. *Chem. Commun.* **2012**, *48*, 9634−9636.

(29) Bao, L.; Zhang, Z. L.; Tian, Z. Q.; Zhang, L.; Liu, C.; Lin, Y.; Qi, B. P.; Pang, D. W. Electrochemical Tuning of Luminescent Carbon Nanodots: From Preparation to Luminescence Mechanism. *Adv. Mater.* **2011**, *23*, 5801−5806.

(30) Ming, H.; Ma, Z.; Liu, Y.; Pan, K. M.; Yu, H.; Wang, F.; Kang, Z. H. Large Scale Electrochemical Synthesis of High Quality Carbon Nanodots and Their Photocatalytic Property. *Dalton Trans.* **2012**, *41*, 9526−9531.

(31) Jeong, H. K.; Colakerol, L.; Jin, M. H.; Glans, P. A.; Smith, K. E.; Lee, Y. H. Unoccupied Electronic States in Graphite Oxides. *Chem. Phys. Lett.* **2008**, *460*, 499−502.

(32) Jeong, H. K.; Lee, Y. P.; Lahaye, R. J. W. E.; Park, M. H.; An, K. H.; Kim, I. J.; Yang, C. W.; Park, C. Y.; Ruoff, R. S.; Lee, Y. H. Evidence of Graphitic AB Stacking Order of Graphite Oxides. *J. Am. Chem. Soc.* **2008**, *130*, 1362−1366.

(33) Blanton, T. N.; Majumdar, D. X-ray Diffraction Characterization of Polymer Intercalated Graphite Oxide. *Powder Diffr.* **2012**, *27*, 104−107.

(34) Zhou, J. G.; Booker, C.; Li, R. Y.; Zhou, X. T.; Sham, T. K.; Sun, X. L.; Ding, Z. F. An Electrochemical Avenue to Blue Luminescent Nanocrystals from Multiwalled Carbon Nanotubes (MWCNTs). *J. Am. Chem. Soc.* **2007**, *129*, 744−745.

(35) Bourlinos, A. B.; Stassinopoulos, A.; Anglos, D.; Zboril, R.; Karakassides, M.; Giannelis, E. P. Surface Functionalized Carbogenic Quantum Dots. *Small* **2008**, *4*, 455−458.

(36) Bourlinos, A. B.; Stassinopoulos, A.; Anglos, D.; Zboril, R.; Georgakilas, V.; Giannelis, E. P. Photoluminescent Carbogenic Dots. *Chem. Mater.* **2008**, *20*, 4539−4541.
(37) Liu, R. L.; Wu, D. Q.; Liu, S. H.; Koynov, K.; Knoll, W.; Li, Q. An Aqueous Route to Multicolor Photoluminescent Carbon Dots Using Silica Spheres as Carriers. *Angew. Chem., Int. Ed.* **2009**, *48*, 4598−4601.
(38) Roeges, N. P. G. A Guide to the Complete Interpretation of Infrared Spectra of Organic Structures. *J. Chem. Educ.* **1995**, *72*, A93.
(39) Raj, A.; Raju, K.; Varghese, H. T.; Granadeiro, C. M.; Nogueira, H. I. S.; Panicker, C. Y. IR, Raman and SERS Spectra of 2-(Methoxycarbonylmethylsulfanyl)-3,5-dinitrobenzene Carboxylic Acid. *J. Braz. Chem. Soc.* **2009**, *20*, 549−559.
(40) Cheng, Y. H.; Tay, B. K.; Lau, S. P.; Shi, X.; Qiao, X. L.; Sun, Z. H.; Chen, J. G.; Wu, Y. P.; Xie, C. S. Influence of Nitrogen Ion Energy on the Raman Spectroscopy of Carbon Nitride Films. *Diamond Relat. Mater.* **2001**, *10*, 2137−2144.
(41) Li, N.; Li, S. X.; Guo, Z. Y.; Zhuang, Z. F.; Li, R.; Xiong, K.; Chen, S. J.; Liu, S. H. Micro-Raman Spectroscopy Study of the Effect of Mid-Ultraviolet Radiation on Erythrocyte Membrane. *J. Photochem. Photobiol., B* **2012**, *112*, 37−42.
(42) Zheng, M.; Liu, S.; Li, J.; Qu, D.; Zhao, H.; Guan, X.; Hu, X.; Xie, Z.; Jing, X.; Sun, Z. Integrating Oxaliplatin with Highly Luminescent Carbon Dots: An Unprecedented Theranostic Agent for Personalized Medicine. *Adv. Mater.* **2014**, *26*, 3554−3560.
(43) Wei, D. C.; Liu, Y. Q.; Wang, Y.; Zhang, H. L.; Huang, L. P.; Yu, G. Synthesis of N-Doped Graphene by Chemical Vapor Deposition and Its Electrical Properties. *Nano Lett.* **2009**, *9*, 1752−1758.
(44) Wang, X. B.; Liu, L. Q.; Zhu, D. B.; Zhang, L.; Ma, H. Z.; Yao, N.; Zhang, B. L. Controllable Growth, Structure, and Low Field Emission of Well-Aligned CN_x Nanotubes. *J. Phys. Chem. B* **2002**, *106*, 2186−2190.
(45) Casanovas, J.; Ricart, J. M.; Rubio, J.; Illas, F.; Jiménez-Mateos, J. M. Origin of the Large N 1s Binding Energy in X-Ray Photoelectron Spectra of Calcined Carbonaceous Materials. *J. Am. Chem. Soc.* **1996**, *118*, 8071−8076.
(46) Kondo, T.; Casolo, S.; Suzuki, T.; Shikano, T.; Sakurai, M.; Harada, Y.; Saito, M.; Oshima, M.; Trioni, M. I.; Tantardini, G. F.; Nakamura, J. Atomic-Scale Characterization of Nitrogen-Doped Graphite: Effects of Dopant Nitrogen on the Local Electronic Structure of the Surrounding Carbon Atoms. *Phys. Rev. B* **2012**, *86*, 035436.
(47) Zhang, Z.; Hao, J. H.; Zhang, J.; Zhang, B. L.; Tang, J. L. Protein as the Source for Synthesizing Fluorescent Carbon Dots by a One-Pot Hydrothermal Route. *RSC Adv.* **2012**, *2*, 8599−8601.
(48) Pan, D. Y.; Zhang, J. C.; Li, Z.; Wu, M. H. Hydrothermal Route for Cutting Graphene Sheets into Blue-Luminescent Graphene Quantum Dots. *Adv. Mater.* **2010**, *22*, 734−738.
(49) Adachi, M.; Murata, Y. Relationship between π-Conjugation Size and Electronic Absorption Spectrum: Novel π-Conjugation Size Dependence of Indoaniline Dyes. *J. Phys. Chem. A* **1998**, *102*, 841−845.
(50) Amali, A. J.; Hoshino, H.; Wu, C.; Ando, M.; Xu, Q. From Metal−Organic Framework to Intrinsically Fluorescent Carbon Nanodots. *Chem.—Eur. J.* **2014**, *20*, 8279−8282.
(51) Upamali, K. A. N. Carbazole-Based, Self-Assembled, Pi-Conjugated Systems as Fluorescent Micro and Nanomaterials—Synthesis, Photophysical Properties, Emission Enhancement and Chemical Sensing. Ph.D. Dissertation, Bowling Green State University, Bowling Green, OH, 2011.
(52) Mahmoud, M. A.; Poncheri, A. J.; El-Sayed, M. A. Properties of π-Conjugated Fluorescence Polymer−Plasmonic Nanoparticles Hybrid Materials. *J. Phys. Chem. C* **2012**, *116*, 13336−13342.
(53) Chen, X. B.; Liu, L.; Yu, P. Y.; Mao, S. S. Increasing Solar Absorption for Photocatalysis with Black Hydrogenated Titanium Dioxide Nanocrystals. *Science* **2011**, *331*, 746−750.
(54) Li, Y. F.; Yin, W. J.; Deng, R.; Chen, R.; Chen, J.; Yan, Q. Y.; Yao, B.; Sun, H. D.; Wei, S. H.; Wu, T. Realizing a SnO2-Based Ultraviolet Light-Emitting Diode Via Breaking the Dipole-Forbidden Rule. *NPG Asia Mater.* **2012**, *4*, e30.
(55) Barnes, W. L. Fluorescence near Interfaces: The Role of Photonic Mode Density. *J. Mod. Opt.* **1998**, *45*, 661−699.
(56) Jenekhe, S. A.; Osaheni, J. A. Excimers and Exciplexes of Conjugated Polymers. *Science* **1994**, *265*, 765−768.
(57) Yu, G.; Yin, S. W.; Liu, Y. Q.; Chen, J. S.; Xu, X. J.; Sun, X. B.; Ma, D. G.; Zhan, X. W.; Peng, Q.; Shuai, Z. G.; Tang, B. Z.; Zhu, D. B.; Fang, W. H.; Luo, Y. Structures, Electronic States, Photoluminescence, and Carrier Transport Properties of 1,1-Disubstituted 2,3,4,5-Tetraphenylsiloles. *J. Am. Chem. Soc.* **2005**, *127*, 6335−6346.
(58) Niu, P.; Zhang, L. L.; Liu, G.; Cheng, H. M. Graphene-Like Carbon Nitride Nanosheets for Improved Photocatalytic Activities. *Adv. Funct. Mater.* **2012**, *22*, 4763−4770.
(59) Auweter, H.; Haberkorn, H.; Heckmann, W.; Horn, D.; Lüddecke, E.; Rieger, J.; Weiss, H. Die Supramolekulare Struktur Ausgefällter, Nanometergroßer B-Carotinpartikel. *Angew. Chem.* **1999**, *111*, 2325−2328.
(60) Auweter, H.; Haberkorn, H.; Heckmann, W.; Horn, D.; Lüddecke, E.; Rieger, J.; Weiss, H. Supramolecular Structure of Precipitated Nanosize Beta-Carotene Particles. *Angew. Chem., Int. Ed.* **1999**, *38*, 2188−2191.
(61) Liang, S. C.; Liu, Y. B.; Xiang, J.; Qin, M.; Yu, H.; Yan, G. P. Fabrication of a New Fluorescent Polymeric Nanoparticle Containing Naphthalimide and Investigation on Its Interaction with Bovine Serum Albumin. *Colloids Surf., B* **2014**, *116*, 206−210.
(62) Chen, N. T.; Cheng, S. H.; Liu, C. P.; Souris, J. S.; Chen, C. T.; Mou, C. Y.; Lo, L. W. Recent Advances in Nanoparticle-Based Forster Resonance Energy Transfer for Biosensing, Molecular Imaging and Drug Release Profiling. *Int. J. Mol. Sci.* **2012**, *13*, 16598−16623.
(63) Wang, X. Y.; He, F.; Zhu, X.; Tang, F.; Li, L. D. Hybrid Silver Nanoparticle/Conjugated Polyelectrolyte Nanocomposites Exhibiting Controllable Metal-Enhanced Fluorescence. *Sci. Rep.* **2014**, *4*, 4406.
(64) Chen, Y.; Munechika, K.; Ginger, D. S. Dependence of Fluorescence Intensity on the Spectral Overlap between Fluorophores and Plasmon Resonant Single Silver Nanoparticles. *Nano Lett.* **2007**, *7*, 690−696.
(65) Narayanan, R.; Deepa, M.; Srivastava, A. K. Forster Resonance Energy Transfer and Carbon Dots Enhance Light Harvesting in a Solid-State Quantum Dot Solar Cell. *J. Mater. Chem. A* **2013**, *1*, 3907−3918.
(66) Kochuveedu, S. T.; Son, T.; Lee, Y.; Lee, M.; Kim, D.; Kim, D. H. Revolutionizing the Fret-Based Light Emission in Core-Shell Nanostructures Via Comprehensive Activity of Surface Plasmons. *Sci. Rep.* **2014**, *4*, 4735.
(67) Michalet, X.; Pinaud, F. F.; Bentolila, L. A.; Tsay, J. M.; Doose, S.; Li, J. J.; Sundaresan, G.; Wu, A. M.; Gambhir, S. S.; Weiss, S. Quantum Dots for Live Cells, in Vivo Imaging, and Diagnostics. *Science* **2005**, *307*, 538−544.
(68) Courty, S.; Luccardini, C.; Bellaiche, Y.; Cappello, G.; Dahan, M. Tracking Individual Kinesin Motors in Living Cells Using Single Quantum-Dot Imaging. *Nano Lett.* **2006**, *6*, 1491−1495.
(69) Cho, E. C.; Zhang, Q.; Xia, Y. N. The Effect of Sedimentation and Diffusion on Cellular Uptake of Gold Nanoparticles. *Nat. Nanotechnol.* **2011**, *6*, 385−391.
(70) Treuel, L.; Jiang, X. E.; Nienhaus, G. U. New Views on Cellular Uptake and Trafficking of Manufactured Nanoparticles. *J. R. Soc., Interface* **2013**, *10*, 20120939.